

INVESTIGATION OF PLUME NON-EQUILIBRIUM INFRARED RADIATION CHARACTERISTICS AT DIFFERENT MACH NUMBERS

Jianyu Xu [1], Li Zhou[1,2,3], Jie Shi[1] , Zhanxue Wang[1,2,3], Hao Shi[1]

[1]School of Power and Energy, Northwestern Polytechnical University, Xi'an 710072, China
[2]National Key Laboratory of Science and Technology on Advanced Light-duty Gas-turbine, Xi'an, 100191, China
[3]Key Laboratory of Digital and Intelligent Technologies for Aero-engine, Ministry of Industry and Information Technology, Xi'an 710072, China

Abstract

The exhaust plume of hypersonic vehicle propulsion systems represents a critical target for signal detection due to its large scale, extensive expansion, and intense radiation signatures. Accurately capturing its flow field and radiation characteristics is therefore of profound significance for detection applications. A non-equilibrium energy-level calculation method for radiating molecules within the plume is established based on molecular dynamics theory. A two-temperature line-by-line (LBL) model and a rapid LBL calculation model based on backpropagation (BP) neural network are developed. Coupled with the backward Monte Carlo method, the infrared radiation characteristics of the thermal non-equilibrium plume were simulated. Based on a modified Navier-Stokes (N-S) equations approach, the proposed non-equilibrium infrared radiation calculation method is employed to investigate the infrared radiation characteristics of a rocket plume at an altitude of 80 km under varying free-stream velocities (Mach 5, 10, 15, 20, and 25).The results indicate that as the free-stream velocity increases, the infrared radiation intensity of the plume initially decreases before subsequently increasing. The compression effect of air shock wave on plume is significantly enhanced. At Mach 25, the maximum lateral dimension of rocket plume is compressed by free stream to 49.2% of its size at Mach 5. The infrared radiation intensity of convergent flow exhibits a similar trend of initial decrease followed by an increase with rising free stream velocity, while the crescent shape in plume's infrared imagery becomes progressively flatter. Furthermore, the distribution characteristics of the rotational temperature within the flow field transition from a "hot flow enveloping cold flow" regime to a "cold flow enveloping hot flow" regime. As freestream velocity increases, vibrational temperature freezing diminishes, vibrational temperature at plume separation shocks rises, and lateral as well as longitudinal expansions are attenuated. As a result, the nozzle diamond shock structure contracts and shifts upstream, core flow expansion is restrained, and maximum expansion Mach number decreases by 40.36%.

Keywords: Rocket plume; Thermal Nonequilibrium Flow; Nonlinear Coupled Constitutive Relations; Line-By-Line Calculation Method; Non-Equilibrium Infrared Radiation;

1.Introdcution

Hypersonic vehicles operate in near space at altitudes ranging from 20 to 100 km, traversing the atmosphere up to Kármán line. Because of this unique flight range, the Earth's curvature renders conventional radar systems ineffective for early warning and detection. Conversely, the exhaust plumes of hypersonic vehicles are characterized by their large scale, drastic expansion, and intense radiation. Consequently, capturing the infrared signatures of these plumes constitutes a critical methodology for the detection of hypersonic vehicles[1]-[3].However, the plume flow field encompasses continuum, transitional, and free molecular flow regimes. Traditional Computational Fluid Dynamics (CFD) methods predicated on the Navier-Stokes (N-S) equations progressively fail as the molecular mean free path increases. The plume demonstrates significant thermal non-equilibrium phenomena and rarefaction effects, which inherently alter the distribution of molecular energy levels. The population densities of high and low energy states deviate from those observed in thermodynamic equilibrium, thereby modifying the absorption and emission characteristics of the molecules [4]. Furthermore, during high-speed flight, the plume undergoes severe compression by the high-velocity free stream, which fundamentally alters the characteristics of this thermal non-equilibrium flow field and its corresponding

radiation signatures. Therefore, investigating the flow field dynamics and infrared radiation characteristics of non-equilibrium, rarefied plumes under conditions of intense compression is of paramount importance for the effective capture of hypersonic vehicle infrared signals.

To characterize the infrared radiation of a plume, it is essential to first acquire accurate flow field characteristics, subsequently establish a robust calculation model that precisely describes these radiation features, and finally determine the plume's radiation signature by integrating radiative transfer mechanisms. At high altitudes, the extremely low ambient atmospheric pressure subjects the engine exhaust to a low-backpressure environment, causing it to undergo rapid expansion and form a characteristic "feather-like" structure [5]. During this drastic expansion, insufficient collision frequencies between plume molecules prevent adequate energy exchange among various internal energy modes, thereby inducing significant thermal non-equilibrium phenomena. To address these non-equilibrium effects, Park[6] proposed two-temperature, three-temperature, and even multi-temperature models to characterize the energy distribution across distinct molecular modes. These models have been extensively applied in the study of exhaust plumes [7] and vehicle flow fields [8].However, with further in-depth research, investigators have observed that as the flight altitude continues to increase, Computational Fluid Dynamics (CFD) methods predicated on the continuum-flow assumption (i.e., the Navier-Stokes equations) exhibit significant deviations from experimental data [9][10]. Consequently, N-S-based numerical methods are inadequate for accurately describing these high-altitude flow phenomena. To precisely capture such flows, researchers have advanced alternative methodologies capable of accurately modeling rarefied flow fields, including Direct Simulation Monte Carlo (DSMC) method [11], Lattice Boltzmann Method (LBM)[12], Unified Gas-Kinetic Wave-Particle (UGKWP) method [13], and Nonlinear Coupled Constitutive Relations (NCCR) theory[14].

To calculate the spectral radiation characteristics of plumes, researchers currently employ techniques such as line-by-line (LBL) method [15], narrow-band model [16], and k-distribution method[17]. These calculations primarily rely on public spectral radiation databases containing line energy information, such as HITEMP[18], HITRAN[19], and GEISA [20]. However, the molecular spectral line data within these databases are fundamentally measured under thermodynamic equilibrium conditions. In the context of non-equilibrium flow fields, where internal energy exchange is incomplete, researchers have indicated that utilizing these databases introduces deviations when describing the population distribution across high and low molecular energy levels. Consequently, corrections must be applied to model the energy level distributions accurately under such non-equilibrium states. To address this, Park [21] developed Non-Equilibrium Air Radiation (NEQAIR) code, advancing the field from equilibrium to non-equilibrium radiation modeling. Subsequently, Hartung [22] developed the LORAN code for calculating non-equilibrium radiation characteristics. Furthermore, Du [23] established a partition function calculation method based on the Boltzmann distribution for vibrational and rotational energy levels. They applied this methodology to compute infrared radiation of the Fatah missile. Their study revealed that at a 90° detection angle, the non-equilibrium radiation intensity within the 4.9~5.9μm band is 1.2 times greater than that predicted by the equilibrium radiation model.

Concurrently, researchers have observed that variations in flight parameters induce significant changes in the structural characteristics of plumes. Peng [24] investigated the infrared radiation of solid rocket motor exhaust plumes under various flight parameters. Their findings indicate that at an altitude of 5 km and within the Mach 1 to 5 range, each increment of Mach 1 results in a 10.1% increase in the plume's axial dimension, a 53.9% decrease in its radial dimension, and an extension of the core flow length. Similarly, Sun [25] analyzed the variation patterns of missile exhaust radiation in relation to flight parameters under distinct flight conditions. They discovered that at a constant flight altitude, an increase in Mach number leads to a reduction in the exhaust plume's boundary layer thickness and a subsequent alteration of the overall plume structure. Furthermore, Alexander [26] examined the dynamics of high-altitude plumes, categorizing the plume into three distinct regions. Research revealed the formation of a gas-dynamic bubble at the center of plume, the cross-sectional area of which expands with increasing altitude, accompanied by a lateral expansion velocity reaching 2 to 3 km/s.

Based on aforementioned studies, it is evident that thermal non-equilibrium and rarefaction effects must be accounted for when computing infrared radiation of high-altitude plumes. While the morphology and characteristics of these high-altitude plumes vary under different free-stream conditions, the influence of these varying structures on thermal non-equilibrium phenomena and rarefaction effects remains scarcely addressed. As the free-stream Mach number increases, the external flow compresses the plume, thereby altering the degree of internal thermodynamic non-

equilibrium. The precise impact of such variations in the non-equilibrium state on infrared radiation characteristics has not yet been thoroughly investigated. Consequently, this paper aims to investigate the variations in the non-equilibrium radiation of plumes under diverse free-stream conditions. By establishing a comprehensive non-equilibrium radiation calculation methodology for plumes—specifically comprising a non-equilibrium flow field solver and a non-equilibrium infrared radiation calculation model—numerical simulations are conducted to analyze the infrared radiation of a booster plume at an altitude of 80 km. This study explores the evolutionary characteristics of the shock wave structure, rotational-vibrational temperatures, and infrared radiation signatures under free-stream Mach numbers of 5, 10, 15, 20, and 25. Furthermore, it seeks to elucidate the underlying mechanisms by which different free-stream velocities affect plume and to uncover the coupling mechanisms between flow field dynamics and infrared radiation variations under these differing velocities. Conducting this research is of profound significance for deepening the understanding of how external free streams influence plume non-equilibrium flow fields and non-equilibrium radiation. Ultimately, this work facilitates the effective detection of hypersonic vehicle infrared radiation signatures across varying flight speeds.

2. Methodology

2.1Flow Field Simulation Method

Based on generalized hydrodynamics theory, Eu [27] established the Nonlinear Coupled Constitutive Relations (NCCR) equations. Building upon Eu's single-component equations, Ahn [28] developed a nonlinear coupled constitutive model encompassing both monatomic and polyatomic molecules. The principal equations are as follows:

$$\frac{\partial}{\partial t}\begin{pmatrix}\rho\\ \rho\mathbf{u}\\ \rho E\\ \rho_i\end{pmatrix}+\nabla\cdot\begin{pmatrix}\rho\mathbf{u}\\ \rho\mathbf{u}\mathbf{u}\\ (\rho E+p)\mathbf{u}\\ \rho_i\mathbf{u}\end{pmatrix}+\nabla\cdot\begin{pmatrix}0\\ \sum_{i=1}^{r}(\boldsymbol{\Pi}_i+\omega\Delta_i\mathbf{I})\\ \sum_{i=1}^{r}(\boldsymbol{\Pi}_i+\omega\Delta_i\mathbf{I})\cdot\mathbf{u}+\mathbf{Q}\\ \frac{\rho_i}{\rho}D_{c,i}c_{c,i}\end{pmatrix}=\begin{pmatrix}0\\ 0\\ 0\\ S_i\end{pmatrix} \tag{1}$$

where: the subscript *i* denotes the physical quantities of a specific species; **u**,*p* and *E* represent the average velocity, pressure, and total energy of the multicomponent gas mixture, respectively; $\boldsymbol{\Pi}$ is the viscous stress; $\boldsymbol{\Delta}$ is the excess normal stress; Q is the heat flux; $D_{c,i}$ is the diffusion coefficient of species *i*; $C_{c,i}$ is the mass fraction of species *i*; and S_i is the chemical reaction source term.

Nondimensionalizing the transport equation yields:

$$\boldsymbol{\Pi}q(cR)=(1+f_b\Delta)\boldsymbol{\Pi}_0+[\boldsymbol{\Pi}\cdot\nabla\boldsymbol{u}]^{(2)} \tag{2}$$

$$\Delta q(cR)=\Delta_0+\frac{3}{2}f_b(\boldsymbol{\Pi}+f_b\Delta\boldsymbol{I}):\nabla\boldsymbol{u} \tag{3}$$

$$\boldsymbol{Q}q(cR)=(1+f_b\Delta)\boldsymbol{Q}_0+\boldsymbol{\Pi}\boldsymbol{Q}_0+\boldsymbol{Q}\nabla\boldsymbol{u} \tag{4}$$

where *c* represents the molecular model parameter; *R* denotes the dimensionless Rayleigh-Onsager dissipation function; $\boldsymbol{\Pi}_0$ is the Newtonian viscous stress;$\boldsymbol{\Delta}_0$ is the linear excess normal stress; and Q_0 is the Fourier heat flux. The coupling of the NCCR model with the generalized hydrodynamic equations constitutes the fundamental theoretical framework of NCCR [29].

By neglecting the excess normal stress—that is, assuming $f_b = 0$ and $\Delta = 0$, the continued evolution of the NCCR equations yields:

$$\begin{aligned}\prod_{NCCR}&=\prod_0+N_\delta\prod_1+N_\delta^2\prod_2+\cdots\\ Q_{NCCR}&=Q_0+N_\delta Q_1+N_\delta^2Q_2+\cdots\end{aligned} \tag{5}$$

where $\boldsymbol{\Pi}_0$ and $\boldsymbol{Q}_0$ denote the Newtonian viscous stress and Fourier heat flux in the Navier-Stokes (N-S) equations, respectively; $\boldsymbol{\Pi}_i$ and $\boldsymbol{Q}_i$ can be regarded as the higher-order terms; and N_δ is a composite coefficient characterizing the relative magnitude of the static gas pressure to the viscous stress, which is defined as:

$$N_\delta\equiv\frac{\eta_r u_r}{p_r L}=\frac{\gamma Ma^2}{\mathrm{Re}} \tag{6}$$

where η_r is the reference kinematic viscosity, u_r is the reference velocity, p_r is the reference pressure,

and L is the characteristic length.

As indicated by Eq. (6), the composite coefficient N_δ is a function of Ma and Re, correlating with both the degree of gas rarefaction and the velocity magnitude. Therefore, in a certain sense, N_δ can be utilized to characterize degree of gas rarefaction or the extent to which the flow deviates from thermodynamic equilibrium. Furthermore, N_δ can serve as a demarcation parameter for distinguishing between rarefied and continuum flows, demonstrating applicability to high Kn number flows. When the gas is in a state of equilibrium, N_δ is relatively small. Under these conditions, the higher-order terms within Π_{NCCR} and Q_{NCCR} in Eq. (5) can be neglected, and the NCCR equations asymptotically reduce to the Navier-Stokes (N-S) equations. Conversely, when the gas flow deviates from equilibrium, the influence of these higher-order terms in Π_{NCCR} and Q_{NCCR} on the viscous stress and heat flux becomes significant and cannot be ignored. Consequently, when computing non-equilibrium rarefied flows, the NCCR equations yield a higher degree of accuracy compared to the N-S equations.

However, the direct numerical solution of the NCCR equations is relatively difficult because the algebraic closure required at each step is significantly more complex than that of the N-S equations [30]. The solution strategies employed by existing solvers lack sufficient robustness in three-dimensional or strongly non-equilibrium scenarios[31], and the discretization or iterative solving processes can introduce spurious instabilities or non-physical solutions[32].

To circumvent the difficulties associated with directly solving NCCR equations, this study proposes a modified approach based on Eq. (5). By leveraging NCCR theory to apply corrections to the N-S equations, results superior to standard N-S solutions can be achieved. The modification procedure is illustrated in Fig. 1, with the principal methodology outlined as follows:

1. Perform an initial computation of flow field utilizing the standard N-S equations to acquire preliminary flow field data.
2. Based on these preliminary results, calculate the composite coefficient N_δ for each computational cell, and establish a scaling coefficient α relating it to the baseline N-S terms $\boldsymbol{\Pi}_0$ and $\boldsymbol{Q}_0$.
3. Utilize the scaling coefficient α to correct the N-S results. Subsequently, iterate this entire procedure repeatedly until convergence is achieved to obtain the final flow field results.

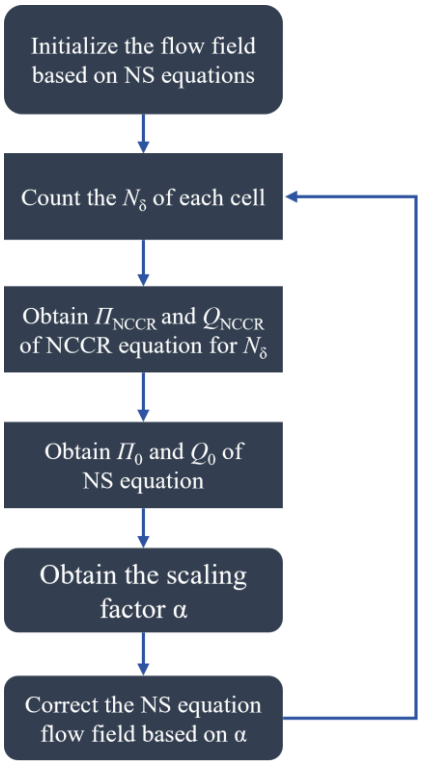


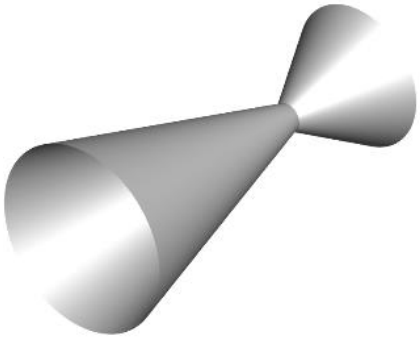
Fig. 1 Flowchart of modifying the Navier-Stokes equations based on the NCCR model

2.2 CFD Method Validation

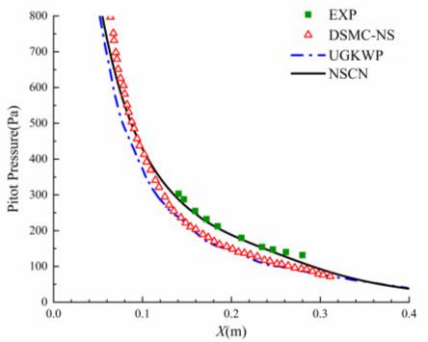
In this section, the expansion of the carbon dioxide plume in the nozzle in a near-vacuum environment was simulated based on reference[33]. The physical model of nozzle based on reference [34]is shown in the Fig.2(a) The stagnation pressure at the nozzle inlet is 4866.18Pa and stagnation temperature is

710K. The ambient pressure P∞ is 0.01Pa and ambient temperature T∞ is 300K. The nozzle wall is isothermal and Tw=500K. Inside the nozzle, the Knudsen number of the nozzle is small enough to approach the continuous flow region, while the outer backflow and plume regions the Knudsen number has reached the free molecular flow region. This multiscale problem can provide a good verification for verifying the flow field capture capability of the calculation method.

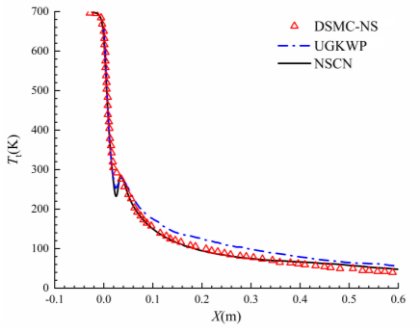
To validate NSCN method, the Pitot pressure, Translational Temperature T_t and Vibrational Temperature Tv along the central axis of nozzle are shown in Fig. 2 which shows the pitot pressure of nozzle centerline, including the experiments results of Bailey[33],DSMC-NS[34],UGKWP[35] and the result of NSCN method in Fig. 2(b). Fig. 2(c) presents the distribution translational temperature of the nozzle centerline by three numerical simulation methods, while Fig. 2(c) shows the translational and vibrational temperature distribution of the nozzle centerline by the NSCN and DSMC-NS As shown in Fig. 2, the NSCN method has reasonable agreements in simulating the near-vacuum plume. The simulation results have great agreement with DSMC-NS and UGKWP. Similar to UGKWP method, NSCN method can also capture the temperature jump at the nozzle throat which showing great accuracy.



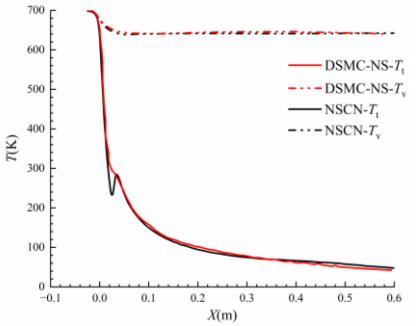
(a)The Geometry shape of the nozzle



(b) Pitot Pressure along the axis of the nozzle



(c) Translational Temperature along the axis of the nozzle



(d) Translational and Vibrational Temperature along the axis of the nozzle

Figure. 2 Temperature and Pitot Pressure Distribution along the axis of nozzle

2.3 Nonequilibrium infrared radiation Method

In the context of molecular infrared radiation, the energy originates from rovibrational energy levels. A molecule possesses multiple vibrational energy levels v, and each vibrational level encompasses multiple rotational energy levels J. Emission and absorption processes occur among these rotational levels, resulting in a multitude of spectral lines. At a specific wavenumber, the spectral absorption coefficient kv is determined by the superposition of these individual spectral lines:

$$\kappa_v = \sum_i \kappa_v^i = \sum_i S_i F(v - v_i) \qquad (7)$$

where $k_v{}^i$ represents the absorption coefficient contributed by spectral line i at a specific wavenumber v; S_i denotes the line strength of spectral line i; and $F(v\text{-}v_i)$ represents the line shape function. Based on the Einstein relations for spectral line absorption and emission, the line strength S_i satisfies the following relation:

$$S_i = \frac{c^2}{8\pi f^2} N_l A_{u\to l} \frac{g_u}{g_l} \left(1 - \exp\frac{-hf}{kT}\right) \qquad (8)$$

where f is the frequency, N_l is the number density of the lower energy state, $A_{u\to l}$ is the Einstein coefficient for spontaneous emission, gu and gl represent the degeneracies of the upper and lower

energy states, respectively, c is the speed of light, h is Planck constant, and k is Boltzmann constant. By substituting the relationship between the number density of the lower energy state and the total molecular number density, Eq. (8) can be rewritten as:

$$S_i = \frac{A_{u\to l}}{8\pi c v^2}\frac{g_u}{Q(T)}\exp(-\frac{E_l}{kT})(1-\exp\frac{-hcv}{kT}) \quad (9)$$

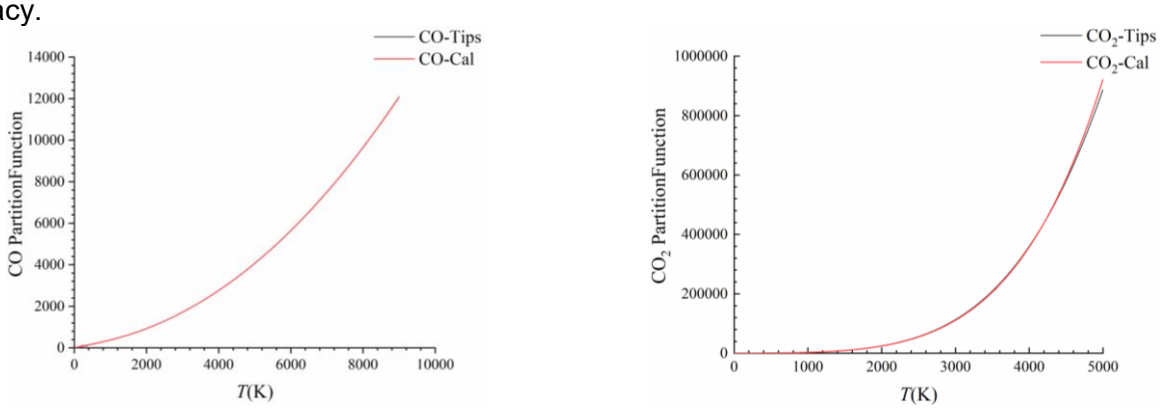
For the calculation of vibrational spectral line strength, the HITEMP database determines the equilibrium spectral line strength S_0 at a given temperature T by scaling it relative to a reference line strength S_i defined at a reference temperature and pressure. The relation is expressed as:

$$\frac{S_i}{S_0(P_0,T_0)} = \frac{\frac{1}{Q(T)}\exp\left(\frac{-c_2E_l}{T}\right)\left[1-\exp(-c_2v/T)\right]}{\frac{1}{Q(T_0)}\exp\left(\frac{-c_2E_l}{T_0}\right)\left[1-\exp(-c_2v/T_0)\right]} \quad (10)$$

where $S_0(P_0,T_0)$ denotes the spectral line strength at the reference pressure P_0 and reference temperature T_0; $Q(T)$ represents the equilibrium partition function at temperature T ; and E_l is the lower-state energy. Equation (9) expresses the equilibrium line strength S_i of spectral line i under the reference conditions P_0 and T_0. From the HITEMP database, parameters such as the reference line strength, lower-state energy, partition function at the reference temperature, and wavenumber can be extracted. By utilizing TIPS to obtain the partition functions at different temperatures, the spectral line strength can be readily calculated via Eq. (10). However, in a non-equilibrium state, owing to the incomplete exchange of rovibrational energy, the internal energy is governed by two temperature components, T_t and T_v. Therefore, the total lower-state energy must be decoupled into two distinct parts: the lower-state rotational energy and the lower-state vibrational energy. Furthermore, the stimulated emission is simultaneously influenced by both the rotational and vibrational temperatures; consequently, the partition function must be jointly determined by these two energy modes. According to Ref[36], under non-equilibrium conditions, Eq. (10) becomes:

$$\frac{S_i}{S_0(P_0,T_0)} = \frac{\frac{1}{Q(T_t,T_v)}\exp\left(\frac{-c_2(E_{lt}+E_{lv})}{T_{ov}}\right)\left[1-\exp(-c_2v/T_{ov})\right]}{\frac{1}{Q(T_0)}\exp\left(\frac{-c_2E_l}{T_0}\right)\left[1-\exp(-c_2v/T_0)\right]} \quad (11)$$

where E_{lt} and E_{lv} denote the lower-state rotational and vibrational energies, respectively; T_{ov} represents the overall temperature; and $Q(T_t,T_v)$ represents the partition function governed by the rotational and vibrational temperatures. The calculations of E_{lt}, E_{lv}, and $Q(T_t,T_v)$ in this study are based on the methodology detailed in Ref[37]. Regarding the established partition function calculation method, Fig. 3 presents a comparison between its calculated results and the equilibrium partition functions obtained from the TIPS database. As illustrated in Fig. 3, the proposed partition function calculation method is in good agreement with the TIPS database under equilibrium conditions, thereby demonstrating high accuracy.



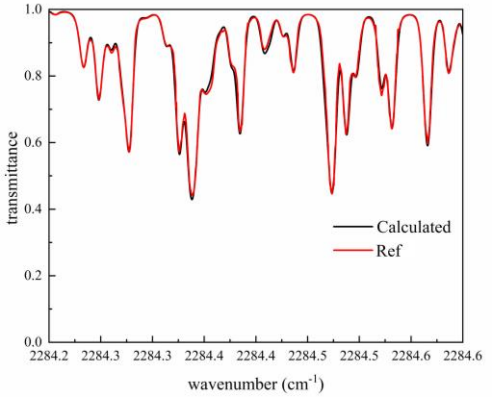
(a)Temperature dependence of CO partition function

(b) Temperature dependence of CO_2 partition function

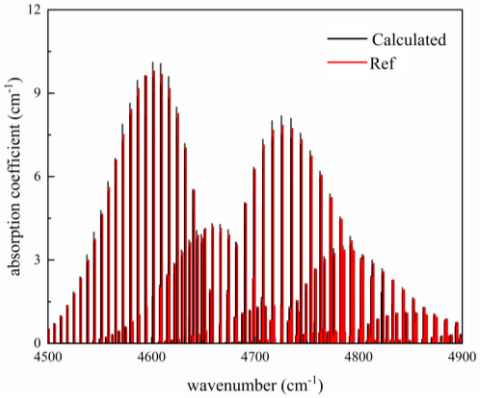
Fig. 3 Comparison of Partition Function between Tips and code

A non-equilibrium line-by-line (LBL) calculation method was developed based on Equation (11) to evaluate the spectral absorption characteristics of CO and CO_2 under rovibrational non-equilibrium states, alongside the equilibrium spectral absorption coefficients of H_2O. Drawing upon data from

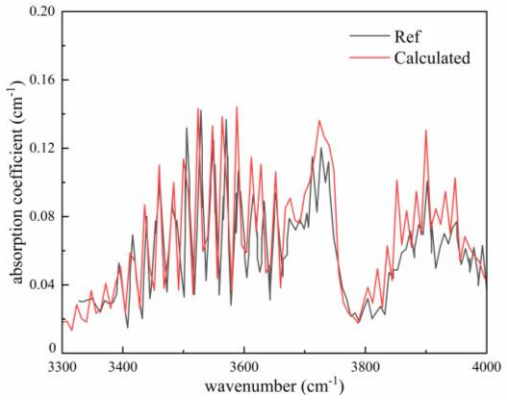
Reference [39]-[41], Figure 4(a) presents a comparison of CO_2 transmittance for T_t = 491K, T_v = 2641K, at a pressure of 20 mbar, a mole fraction of 0.0657, and a path length of 10 cm. Similarly, Figure 4(b) contrasts the absorption coefficients of CO at Tt = 300 K, Tv = 2000 K, and 0.01 bar, while Figure 4(c) details the absorption coefficients for pure H_2O at 1200 K and 1 atm. By benchmarking the computed transmittance and absorption coefficients against established literature, the accuracy and reliability of the proposed non-equilibrium LBL methodology are comprehensively validated.



(a)validation of CO_2 transmittance



(b)validation of CO absorption coefficient



(c)validation of H_2O absorption coefficient at 3300cm^{-1}~4000cm^{-1}

Fig 4. Validation of CO_2 、 CO and H_2O Absorption characteristics

The standard line-by-line calculation is highly accurate but computationally expensive for infrared radiation evaluation due to the millions of spectral lines in databases like HITEMP/HITRAN. To enhance computational speed, a non-equilibrium calculation model powered by a backpropagation (BP) neural network was established. Extending an equilibrium network (which inputs pressure, temperature, and concentration) to a non-equilibrium model requires adding a fourth parameter. However, the lack of complete independence between vibrational and rotational temperatures in two-temperature models significantly complicates a direct neural network approach. Therefore, we constructed a composite architecture featuring an equilibrium neural network coupled with a non-equilibrium partition function layer. By inputting pressure (P), overall temperature (Tov), and species concentration (n), the network first estimates equilibrium spectral absorption coefficient. The non-equilibrium partition function layer then applies a correction to generate the final non-equilibrium coefficient. Developed in C++ to balance efficiency and precision, the BP network calculates 867 output values across the 2–15 μm spectrum at 5 cm^{-1} intervals. Using Sigmoid activation, the network is structured with 3 input nodes, four hidden layers and 867 output nodes. The model's framework is shown below:

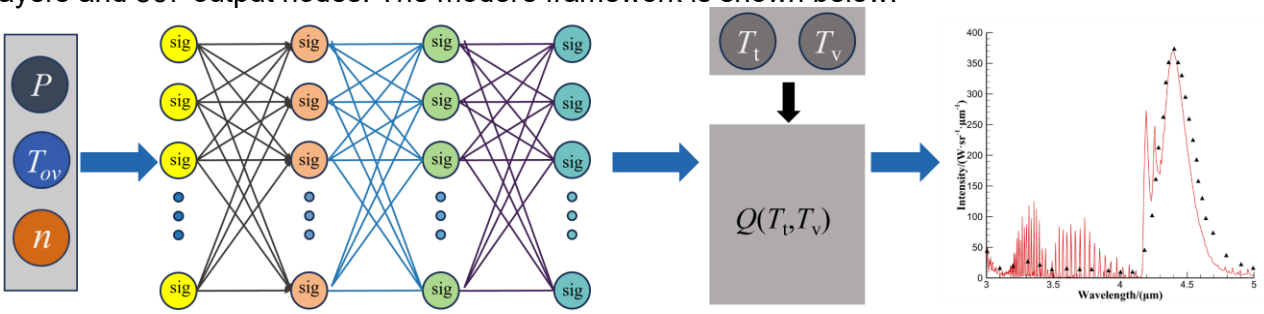


Figure 5. Non-equilibrium neural network line-by-line calculation model.

To validate the proposed non-equilibrium infrared radiation calculation method, a comprehensive analysis of the neural network's prediction accuracy was conducted. A test dataset comprising 10,000 randomly generated samples was utilized. The model yielded an MAE of 0.00124351, an MSE of 0.00000735, an RMSE of 0.00271145, and an R^2 of 0.99877123 across the test data. These metrics demonstrate an excellent overall fit and high predictive precision, confirming that the proposed methodology can accurately capture infrared spectral radiation characteristics. To model the radiative transfer process, the Backward Monte Carlo Method(BMCM) was employed. Grounded in statistical theory, this approach traces rays in reverse from detector to target, calculating the accumulated infrared radiation features along the optical path.

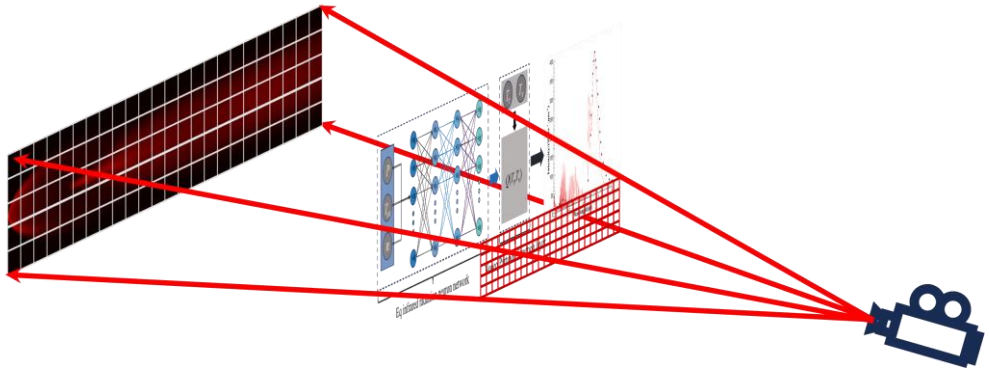


Figure 6. Illustration of BMCM Transmission process

3. Results and discussions

3.1 Numerical Simulation Model and Boundary Conditions

During the ascent and boost phase of hypersonic vehicles, the infrared radiation signature of the exhaust plume is predominantly governed by the booster. Consequently this study selects the RD180 liquid rocket engine—fueled by rocket kerosene (RP-1) and liquid oxygen (LOX)—and models it utilizing a single-nozzle equivalent approach. The equivalent nozzle radius is defined as R = 1.049 m, with an exit static pressure of 70065 Pa, a static temperature of 1935 K, and an exit velocity of 3340 m/s. The exhaust gas consists of H_2O, CO, CO_2, and N_2, with corresponding mole fractions of 0.284, 0.240, 0.470, and 0.006. For boost-glide hypersonic vehicles, the boost phase generally spans an altitude range of 50 to 100 km, with separation altitudes varying according to specific vehicle designs. Therefore, an altitude of 80 km, representing a regime characterized by substantial variations in flight energy, was established as the research baseline. This baseline is utilized to investigate the evolutionary trends of non-equilibrium infrared radiation characteristics of exhaust plume across Mach numbers of 5, 10, 15, 20, and 25.

The computational domain and boundary conditions for the RD-180 are illustrated in Figure xx. The far-field encompasses three distinct zones: far-field inlet, nozzle region, and far-field outlet. Given the severe expansion of the exhaust plume at an altitude of 80 km, the dimensions of far-field domain were established with a radius of 1000 m and a longitudinal length of 6000 m. Following a rigorous grid independence study, a final mesh consisting of 5.88 million elements was adopted.

Given the extreme altitudes associated with high-altitude plumes, real-world observations are typically conducted from long stand-off distances. Consequently, the detection point for evaluating the infrared radiation characteristics in this study is strategically positioned at the exact lateral (broadside) aspect of the plume exhaust. This research specifically investigates the infrared radiation signatures from this normal lateral viewing angle.

3.2 Results and Analysis

To facilitate a preliminary investigation into flow field and infrared radiation characteristics of plume under rarefied conditions, Figure 7 provides the Mach number contour on symmetry plane for a baseline freestream Mach number of 15. In the high-altitude regime, the exhaust plume expands violently upon exiting the nozzle into a low-pressure environment. Simultaneously, this expanding plume encounters the high-velocity freestream, subjecting it to severe freestream compression. Governed by the competing aerodynamic effects of core flow expansion and freestream compression, the plume flow field distinctly partitions into three primary zones: (1) secondary core flow, situated between air shock and plume shock; (2) core flow, bounded by plume shock; (3) post-shock convergent flow, generated downstream of the diamond shock structures. The secondary core flow sustains an

elevated temperature profile as a direct result of freestream compression. Conversely, the central core flow experiences rapid expansion against the diminished back-pressure, which accelerates the flow to exceptionally high velocities, peaking at Mach 25 for a freestream Mach number of 15. As a thermodynamic consequence of this extreme expansion, the temperature of the core flow drops significantly below that of both the secondary core and the convergent flows. Upon traversing the shock structures, the central core flow coalesces downstream of the diamond shocks, giving rise to the high-temperature post-shock convergent flow. Figure 8 maps the infrared radiance of plume at a freestream Mach number of 15. The contour clearly demonstrates that the infrared emissions predominantly originate from the post-shock convergent flow and the secondary core flow (which undergoes severe compression between the jet and freestream shocks). In contrast, the infrared radiation emitted from the rapidly expanding central core flow remains comparatively minimal.

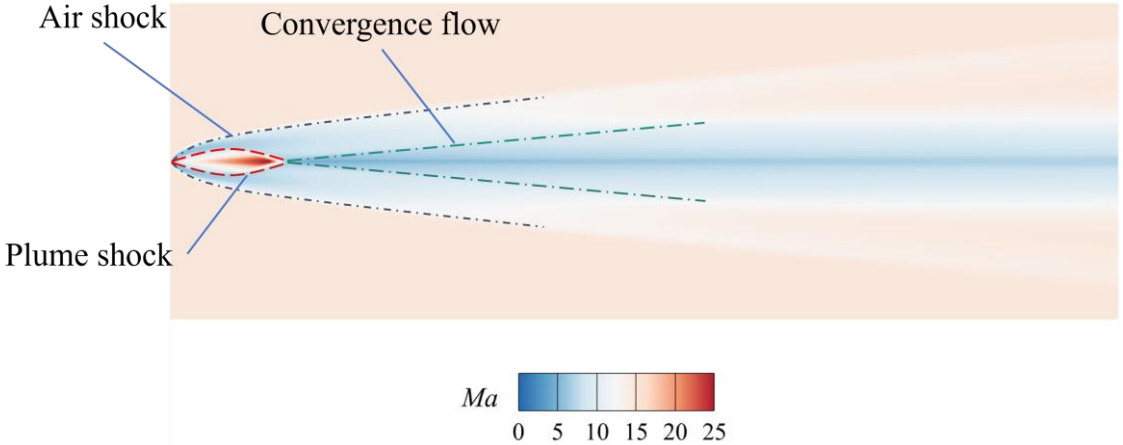


Figure 7. Mach number contour on symmetry plane for Mach 15.

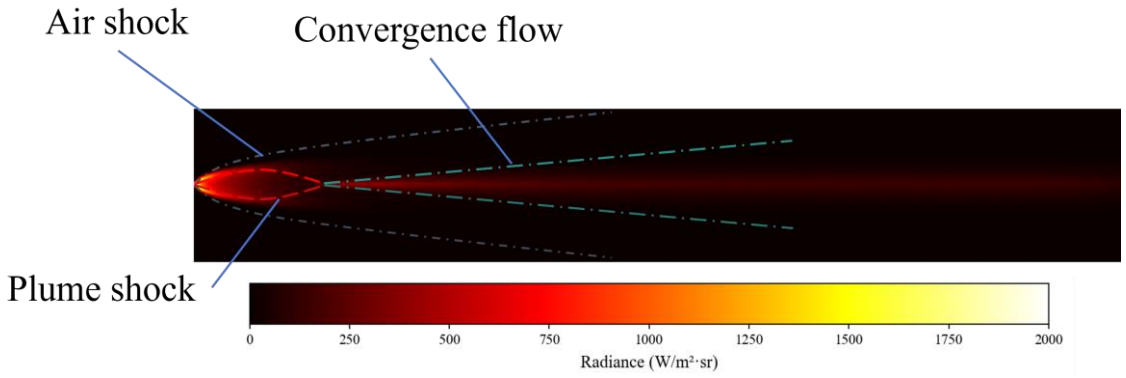
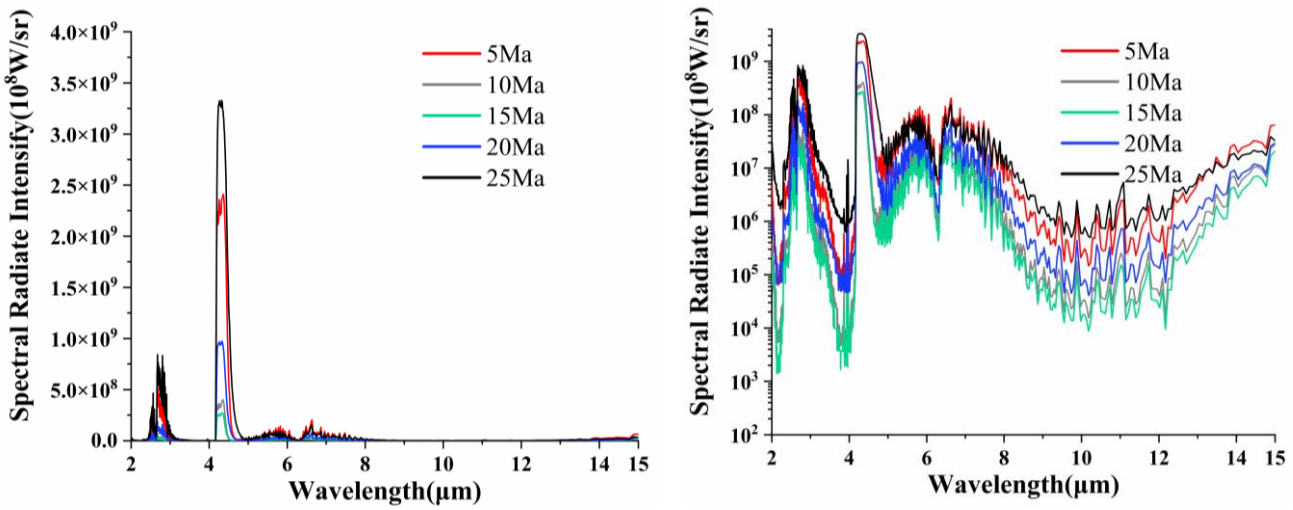


Figure 8. Mach number contour on symmetry plane for Mach 15.

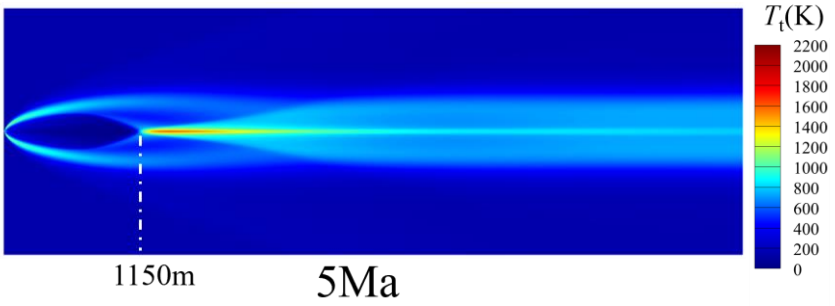
To investigate the infrared radiation characteristics of the plume across various freestream Mach numbers, Figure 10 presents the infrared radiation intensity distribution of the exhaust plume at a 90° detection angle. Specifically, Figure 9(a) illustrates the absolute radiation intensity, while Figure 9(b) displays the logarithmic spectral radiation intensity as a function of wavenumber. As depicted in Figure 10, the primary infrared emission bands of the plume are centered around 2.7 μm, 4.2 μm, and 6.1 μm, with the peak intensity occurring near 4.2 μm. Notably, the radiation signature of CO_2 is markedly more pronounced than those of CO and H_2O. Furthermore, as the freestream Mach number increases, the overall infrared radiation intensity of the plume exhibits a non-monotonic trend, initially decreasing before subsequently increasing. The radiation intensity reaches its absolute minimum at a freestream Mach number of 15; however, as the Mach number continues to rise, the emission intensity at Mach 25 ultimately surpasses that observed at Mach 5.



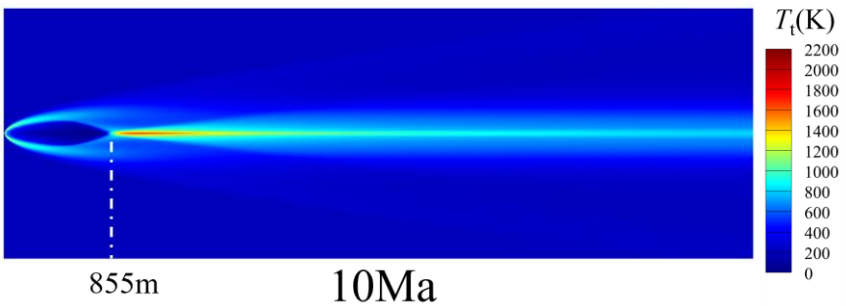
(a) Absolute spectral radiation intensity (b) Logarithmic spectral radiation intensity

Figure 9. Infrared radiation intensity distribution of plume under different freestream Mach

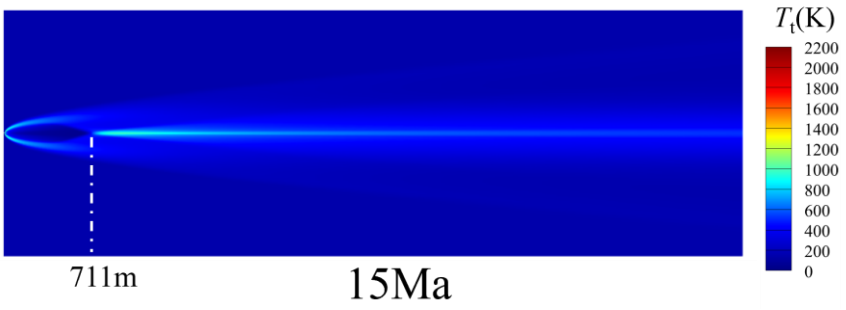
The varying degrees of freestream compression by plume at different Mach numbers significantly alter its flow field, which in turn modifies its infrared radiation intensity. Figure 10 illustrates the rotational temperature T_t contours of plume across various Mach numbers. Additionally, recalling Figure 8, the interaction between the exhaust plume and the ambient atmosphere at the altitude of 80 km induces the formation of both a air shock and a plume shock. As Mach number escalates, the air shock intensifies, leading to a progressive reduction in both the transverse and longitudinal expansion dimensions of the plume. Notably, at Mach 25, the maximum longitudinal dimension of the plume is compressed to just 49.2% of its size at Mach 5. Figure 11 displays the x-direction density gradients of the flow field at Mach 5 and Mach 25. It is evident from this figure that the angle between air shock and plume core flow narrows significantly as the Mach number rises. Consequently, the expansion of the core flow is heavily constrained, and its spatial domain shrinks continuously. This aerodynamic restriction accounts for the phenomenon observed in Figure 11, where the dimensions of the core flow monotonically decrease with an increasing Mach number. Intriguingly, despite the severe spatial restriction of the core flow, the corresponding infrared radiation intensity exhibits a non-monotonic trend—initially decreasing before subsequently increasing at higher Mach numbers. This complex behavior is fundamentally governed by the dynamic trade-off between compressive forces of freestream and expansive forces of plume.



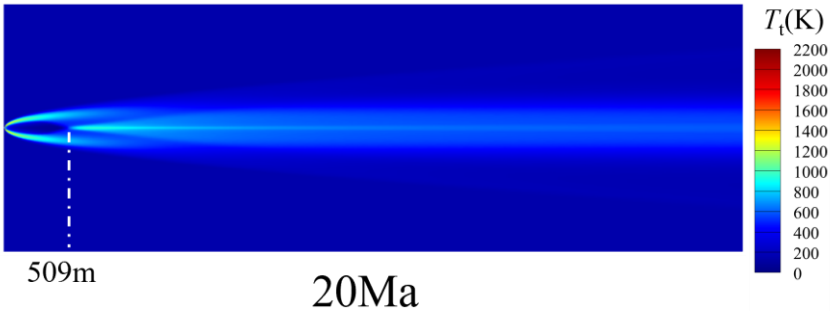
(a)5Ma T_t distribution



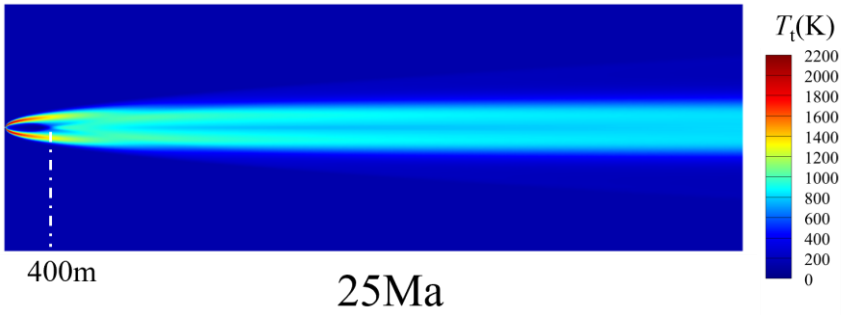
(b)10Ma T_t distribution



(c)15Ma T_t distribution



(d)20Ma T_t distribution



(e)25Ma T_t distribution

Figure 10. Translational temperature contours on symmetry plane across various freestream Ma

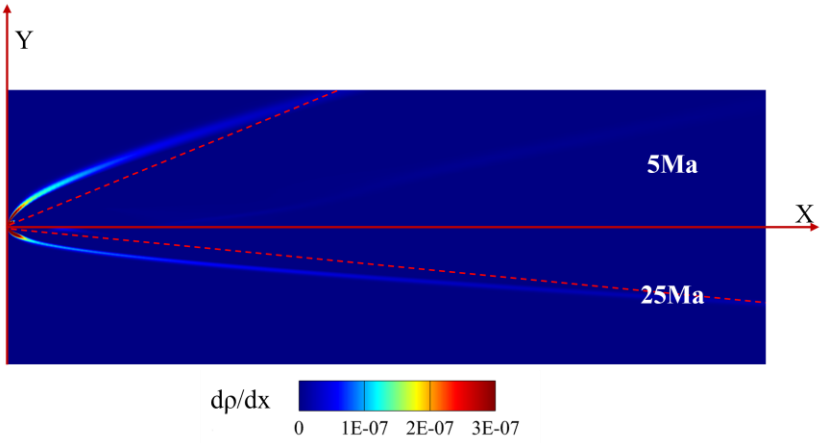
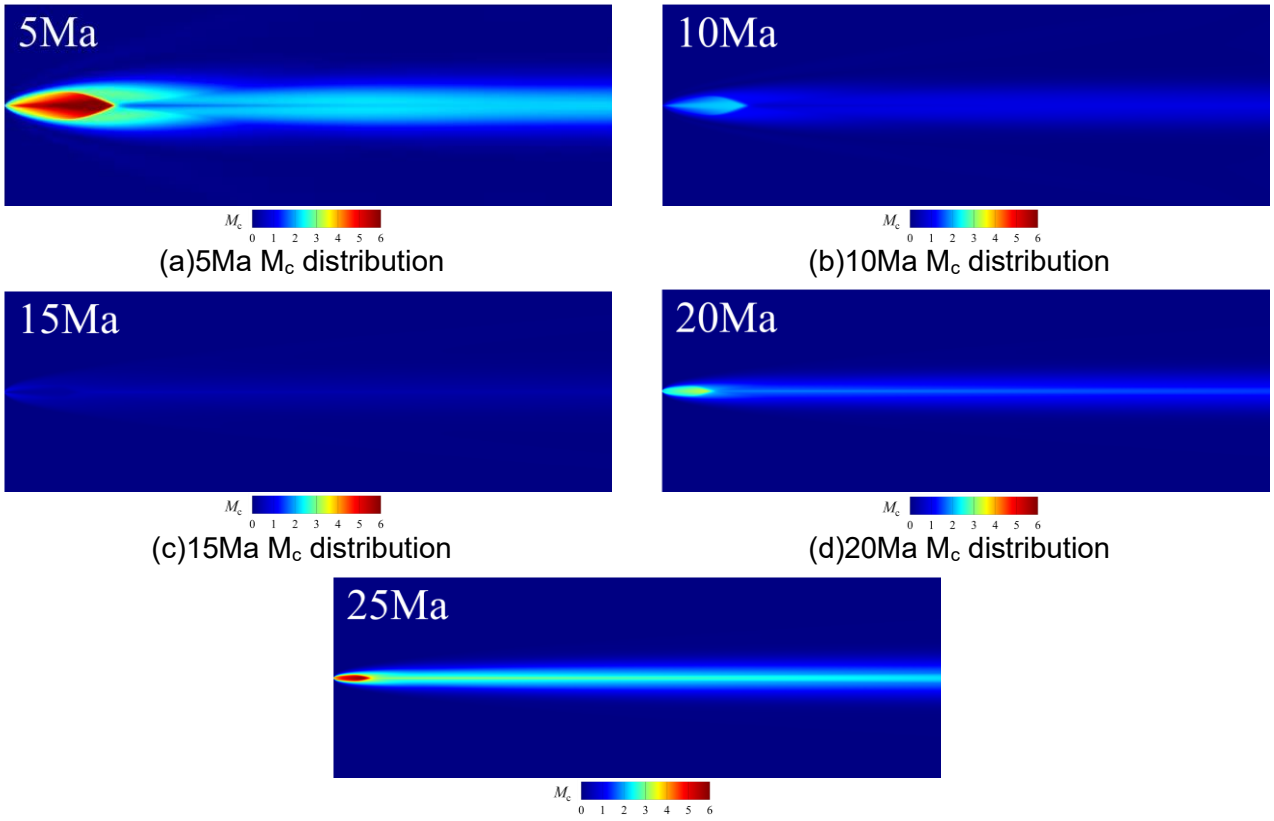


Figure 11. X-direction density gradients

As freestream Mach number increases, the spatial dimensions of core flow and the secondary core flow progressively contract. Concurrently, their rotational temperatures exhibit a non-monotonic trend, initially decreasing before subsequently rising. This phenomenon is fundamentally governed by the competing aerodynamic effects of freestream shock compression and core flow expansion acting upon the secondary core flow. To quantify these respective influences, Figure 12 presents the local convective Mach number contours on the symmetry plane. The convective Mach number is mathematically defined by Equation (12), where Uj and U∞ denote the local and freestream velocities, and aj and a∞ represent the local and freestream speeds of sound, respectively. As the freestream Mach number increases from 5 to 25, the convective Mach number experiences an initial decrease followed by a subsequent increase. At a freestream Mach number of 5, the convective Mach number is relatively high and exhibits a broad spatial distribution. In this regime, the flow field is dominated by

plume expansion, and the influence of freestream on plume is marginal compared to the expanding plume. However, as the Mach number reaches 10, the convective Mach number decreases, and the dominance of the plume expansion diminishes. This attenuation mitigates the compression exerted by core flow onto the secondary core flow, thereby causing a reduction in temperature of secondary flow. Upon further increasing the Mach number to 15, the convective Mach number reaches its minimum, signifying a transition where the freestream begins to dominate flow field. Nevertheless, because its value is lower than that at Ma=10, the freestream-induced compression on secondary core flow is weaker than the compression driven by plume expansion at Mach 10; consequently, the rotational temperature drops below the value observed at Mach 10. As the freestream Mach number continues to elevate, the convective Mach number increases concurrently, and the compressive effect of the freestream on secondary core flow becomes increasingly pronounced. In this phase, the expansion effect of plume is overshadowed by freestream, leading to enhanced compression of secondary core flow and a precipitous rise in its rotational temperature. Ultimately, at a Mach number of 25, the freestream compression on secondary core flow attains its maximum. This results in the highest peak value of convective Mach number and maximum localized temperature. Correspondingly, as illustrated in Figure 10, Tt is significantly elevated compared to the Mach 20 case, yielding a further intensified infrared radiation signature.

$$M_c = \frac{|U_j - U_\infty|}{a_j + a_\infty} \tag{12}$$



(a)5Ma M_c distribution (b)10Ma M_c distribution

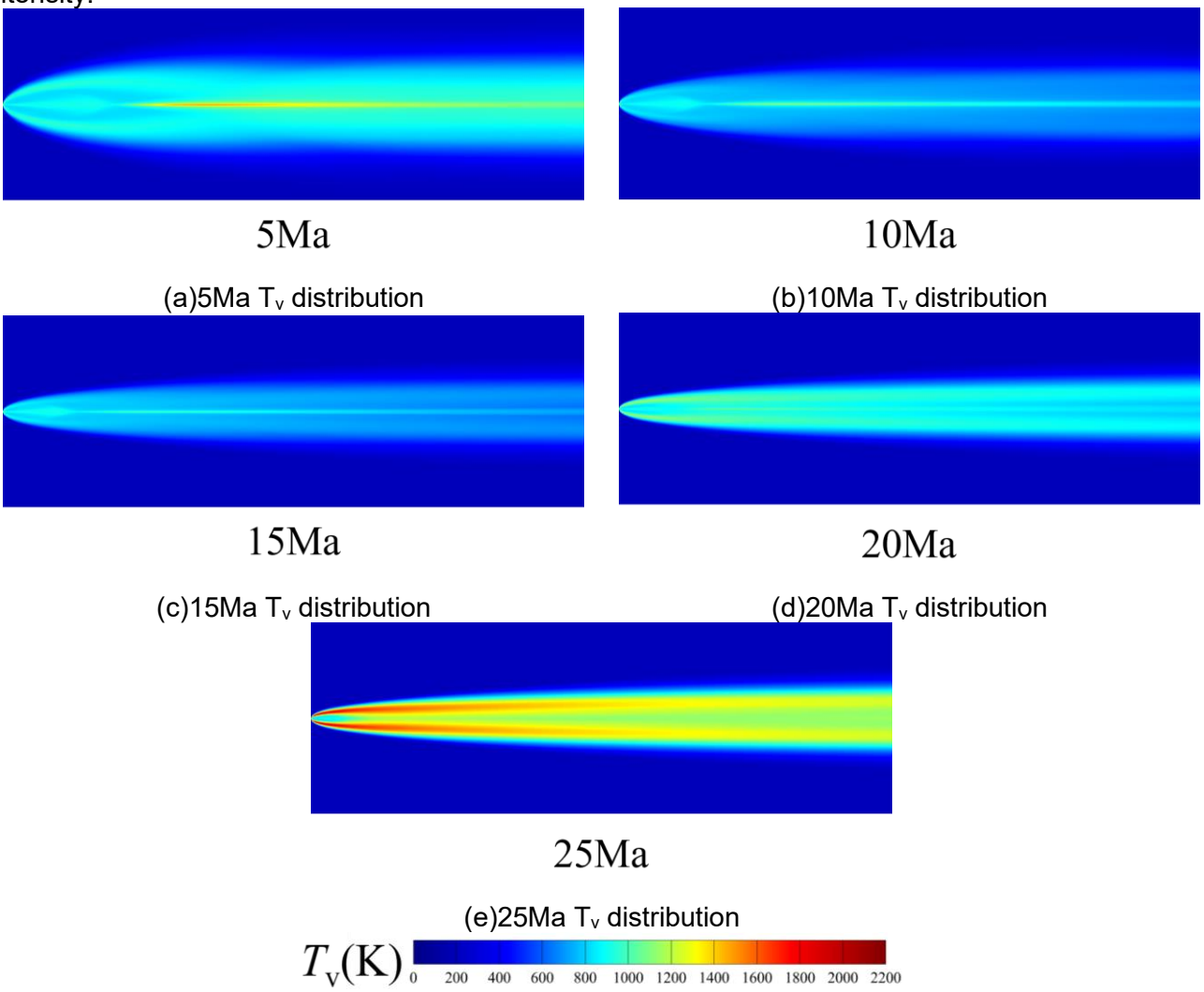
(c)15Ma M_c distribution (d)20Ma M_c distribution

(e)25Ma M_c distribution

Figure 12. Local convective Mach number contour on the symmetry plane.

As freestream Mach number escalates, the governing aerodynamic mechanism of plume gradually shifts from plume expansion to freestream compression. This transition diminishes the expansive forces of plume, causing core flow to be severely compressed by freestream. This compression has a dual effect: it restricts the expansion of core flow—thereby altering its rotational temperature—and it modifies the overall rarefaction of plume, which directly impacts infrared radiation signature. Figure 13 displays vibrational temperature contours of plume across various freestream Mach numbers. It is evident from Figure 13 that as freestream Mach number rises, vibrational temperature similarly follows a non-monotonic trend, initially decreasing before subsequently increasing. However, at higher Mach numbers, the freezing phenomenon of vibrational temperature is progressively attenuated. This attenuation occurs because the constrained plume can no longer fully expand; instead, it is violently squeezed by freestream, which reduces rarefaction levels within both the core and secondary core

flows. To further illustrate this, Figure 14 plots the radial Kn distribution at an axial distance of 200 m from the nozzle exit across different Mach numbers. The data reveal that as freestream Mach number increases, the local Kn number steadily declines. Consequently, the plume transitions closer to a continuum flow regime, leading to a higher frequency of intermolecular collisions. This enhanced collisionality inherently weakens the vibrational temperature freezing effect. At Mach 25, the vibrational temperature demonstrates continuous, synchronized variations as flow field develops downstream. Ultimately, as the freestream Mach number increases, both translational-rotational temperature (Tt) and vibrational temperature (Tv) exhibit an initial decrease followed by an increase. Consequently, the overall reference temperature (Tov) mirrors this non-monotonic trend. These fundamental thermal variations serve as the primary driving mechanism behind the observed changes in infrared radiation intensity.



(a)5Ma T_v distribution (b)10Ma T_v distribution

(c)15Ma T_v distribution (d)20Ma T_v distribution

(e)25Ma T_v distribution

Figure 13. T_v contour on the symmetry plane.

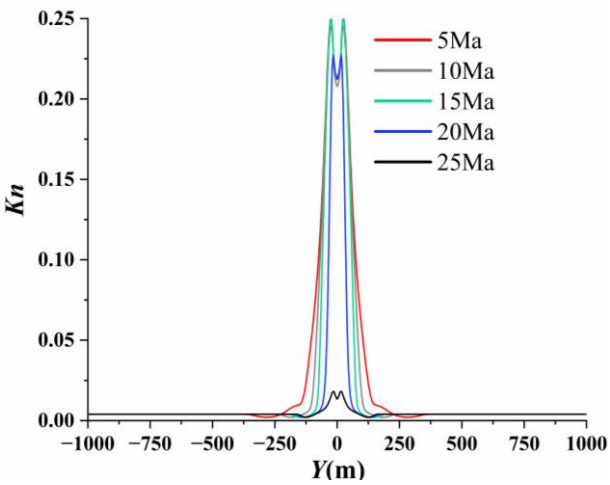
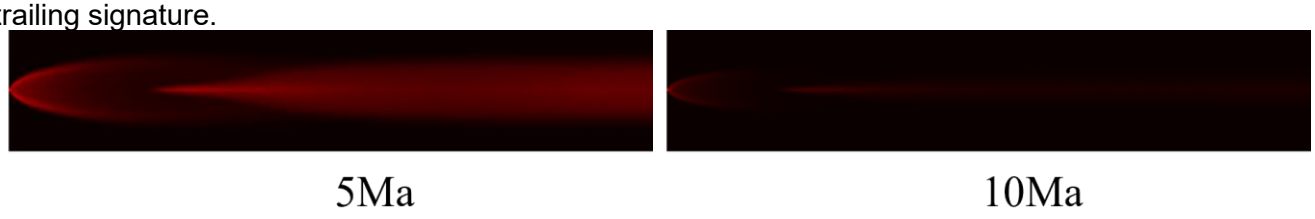


Figure 14. Radial Knudsen (Kn) number distribution at an axial distance of X = 400 m.

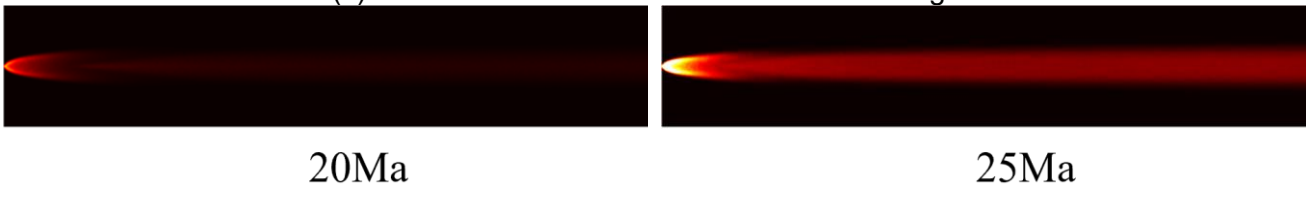
To further investigate how spatial distribution of infrared radiation contributions across different plume regions shifts with varying freestream Mach numbers, Figure 15 presents the infrared radiation imagery of exhaust plume across a range of Mach numbers. At the freestream Mach number of 5, plume's infrared signature exhibits a distinct crescent and spike morphology; here, the infrared radiation is predominantly generated by secondary core flow and post-shock convergent flow. As the Mach number escalates to 10, the downstream "spike" radiation gradually attenuates, leaving secondary core flow as the primary source of radiation. This occurs because the escalating freestream Mach number increasingly compresses core flow, thereby weakening its expansion. This diminished expansion consequently weakens diamond shock structures and lowers the temperature of convergent flow. As a result, the radiant emission from the convergent flow drops, rendering the spike-like signature largely invisible—a phenomenon that persists up to Mach 15. As the Mach number continues rise to 20, the freestream compression acting upon the core flow intensifies severely, subjecting secondary core flow to extreme compression by air shock. Consequently, as observed at Mach 25 in Figure 15, the temperature of secondary core flow surges. This superheated secondary core flow subsequently propagates downstream. Along this trajectory, it vigorously mixes with convergent flow, and the two flows travel downstream in tandem. This mixing substantially elevates both the rotational and vibrational temperatures within the wake flow field. Ultimately, at Mach 25, the far-field wake radiation of plume drastically surpasses that observed at lower Mach regimes, resulting in most pronounced trailing signature.



(a) Freestream Mach 5 infrared radiance image (b) Freestream Mach 10 infrared radiance



(c) Freestream Mach 15 infrared radiance image



(d) Freestream Mach 20 infrared radiance (e) Freestream Mach 25 infrared radiance

Figure 15. Infrared radiance imagery of the exhaust plume across various freestream Mach numbers.

4. Conclusions

Utilizing a comprehensive multi-temperature non-equilibrium infrared radiation modeling framework, this research evaluated the evolutionary trends of plume infrared signatures across a range of Mach numbers. Following a detailed investigation of flow field and radiation characteristics at a baseline Mach number of 15, a comparative analysis was performed for Mach numbers 5 through 25. The conclusions are as follows:

1. The high-altitude plume flow field is partitioned into three primary zones: a secondary core flow region subjected to both freestream and core flow compression, a core flow undergoing rapid expansion into low-pressure environment, and a convergent wake flow generated by the diamond shock structures. At the baseline Mach number, infrared emissions predominantly originate from secondary core and convergent wake regions, where CO_2 and H_2O constitute the primary radiating species, producing a distinct "crescent-and-spike" infrared signature.
2. The total infrared radiation intensity exhibits a non-monotonic "decrease-then-increase" trend as the freestream Mach number escalates, which is governed by competing effects of freestream compression and core flow expansion acting upon secondary core flow. Core expansion is the governing mechanism at lower Mach regimes, whereas freestream compression becomes dominant at higher Mach numbers, driving the thermal and radiative recovery of the secondary core flow.
3. While the secondary core flow and convergent wake remain largely distinct at moderate Mach numbers, they undergo vigorous mixing at Mach 25. This interaction drastically enhances the infrared signature of the far-field wake, manifesting as a significant trailing effect with high-intensity infrared emissions.

5. Contact Author Email Address

mailto: Jianyuxu@mail.nwpu.edu.cn

6. Copyright Statement

The authors confirm that they, and/or their company or organization, hold copyright on all of the original material included in this paper. The authors also confirm that they have obtained permission, from the copyright holder of any third party material included in this paper, to publish it as part of their paper. The authors confirm that they give permission, or have obtained permission from the copyright holder of this paper, for the publication and distribution of this paper as part of the ICAS proceedings or as individual off-prints from the proceedings.

Acknowledgements

This study was co-supported by the National Natural Science Foundation of China (No. 52376032) and the National Science and Technology Major Project, China (No. J2019-Ⅱ-0015-0036).

References

[1]. Karako T, Dahlgren M. Complex air defense: Countering the hypersonic missile threat[M]. Bloomsbury Publishing PLC, 2022.
[2]. Fontana S, Di Lauro F. An overview of sensors for long range missile defense[J]. Sensors, 2022, 22(24): 9871.
[3]. Law Y W, Gliponeo J J, Singh D, et al. Detecting and tracking hypersonic glide vehicles: A cybersecurity-engineering analysis of academic literature[C]//International Conference on Cyber Warfare and Security. Academic Conferences International Limited, 2023: 189-XIV.
[4]. Cai C, Wang L. Numerical validations for a set of collisionless rocket plume solutions[J]. Journal of Spacecraft and Rockets, 2012, 49(1): 59-68.
[5]. Kogan M N. Rarefied gas dynamics[M]. Springer, 2013.
[6]. Parker J G. Rotational and vibrational relaxation in diatomic gases[J]. The Physics of Fluids, 1959, 2(4): 449-462.
[7]. Xubo D U, Qingzhen Y, Haoqi Y, et al. Infrared radiation characteristics of dagger-type hypersonic missile[J]. Chinese Journal of Aeronautics, 2024, 37(4): 137-150.
[8]. Lv J, Hong Q, Wang X, et al. Two-temperature thermochemical nonequilibrium model based on the coarse-grained treatment of molecular vibrational states[J]. Physical Review E, 2024, 110(3): 035107.
[9]. Lofthouse A J, Boyd I D, Wright M J. Effects of continuum breakdown on hypersonic aerothermodynamics[J]. Physics of Fluids, 2007, 19(2).
[10]. Holman T, Boyd I. Numerical investigation of the effects of continuum breakdown on hypersonic vehicle

surface properties[C]//40th Thermophysics Conference. 2008: 3928.
[11]. G. A. Bird. Molecular Gas Dynamics[M].Clarendon Press, Oxford, 1976.
[12]. Wolf-Gladrow D A. Lattice-gas cellular automata and lattice Boltzmann models: an introduction[M]. Springer, 2004.
[13]. Liu C, Zhu Y, Xu K. Unified gas-kinetic wave-particle methods I: Continuum and rarefied gas flow[J]. Journal of Computational Physics, 2020, 401: 108977.
[14]. Myong R S. A computational method for Eu's generalized hydrodynamic equations of rarefied and microscale gasdynamics[J]. Journal of Computational Physics, 2001, 168(1): 47-72.
[15]. Beier K, Lindermeir E. Comparison of line-by-line and molecular band IR modeling of high altitude missile plume[J]. Journal of Quantitative Spectroscopy and Radiative Transfer, 2007, 105(1): 111-127.
[16]. Blunck D L, Gore J P. Study of narrowband radiation intensity measurements from subsonic exhaust plumes[J]. Journal of Propulsion and Power, 2011, 27(1): 227-235.
[17]. Modest M F. Narrow-band and full-spectrum k-distributions for radiative heat transfer—correlated-k vs. scaling approximation[J]. Journal of Quantitative Spectroscopy and Radiative Transfer, 2003, 76(1): 69-83.
[18]. Gordon I E, Rothman L S, Hill C, et al. The HITRAN2016 molecular spectroscopic database[J]. Journal of quantitative spectroscopy and radiative transfer, 2017, 203: 3-69.
[19]. Rothman L S, Gordon I E, Barber R J, et al. HITEMP, the high-temperature molecular spectroscopic database[J]. Journal of Quantitative Spectroscopy and Radiative Transfer, 2010, 111(15): 2139-2150.
[20]. Delahaye T, Armante R, Scott N A, et al. The 2020 edition of the GEISA spectroscopic database[J]. Journal of Molecular Spectroscopy, 2021, 380: 111510.
[21]. Park C. On convergence of computation of chemically reacting flows[J]. // 23rd Aerospace Sciences Meeting. AIAA 1985-247.
[22]. Hartung L C. Nonequilibrium radiative heating prediction method for aeroassist flowfields with coupling to flowfield solvers[M]. North Carolina State University, 1991.
[23]. Du X, Shi Y, Yang Q, et al. Numerical Simulation of Spectral Radiation for Hypersonic Vehicles[J]. Aerospace, 2024, 11(10): 802.
[24]. Peng M, Zou Y, Zhang R, et al. A Study on the Influence of Flight Parameters on Two-Phase Flow and Radiation in the Plume of Solid Rocket Motors[J]. Aerospace, 2025, 12(8): 711.
[25]. Sun Z, Xu, He G. Effect of flight status parameters on missile motor plume[J]. Journal of Solid Rocket Technology, 2005, 28(3): 188.
[26]. Molchanov A G, Platov Y V. Gas dynamics of a rocket plume in the upper atmosphere[J]. Journal of Russian Laser Research, 2010, 31(5): 410-414.
[27]. Eu B C. Kinetic theory and irreversible thermodynamics[J]. NASA STI/Recon Technical Report A, 1992, 93: 24498.
[28]. Ahn J W, Kim C. An axisymmetric computational model of generalized hydrodynamic theory for rarefied multi-species gas flows[J]. Journal of Computational Physics, 2009, 228(11): 4088-4117.
[29]. Myong R S. A generalized hydrodynamic com-putational model for rarefied and microscale dia-tomic gas flows[J]. Journal of Computational Physics, 2004, 195(2): 655-676
[30]. Zeng S, He Z, Zhao W, et al. A computational strategy for nonlinear coupled constitutive relations of rarefied nonequilibrium flows on unstructured grids[J]. Aerospace Science and Technology, 2023, 141: 108477.
[31]. Jiang Z, Zhao W, Chen W, et al. An undecomposed hybrid algorithm for nonlinear coupled constitutive relations of rarefied gas dynamics[J]. Commun. Comput. Phys., 2019, 26(3): 880.
[32]. Cao J, Liu S, Zhong C, et al. Multiple solutions of nonlinear coupled constitutive relation model and its rectification in non-equilibrium flow computation[J]. Computers & Mathematics with Applications, 2024, 174: 1-17.
[33]. Bailey A B, Price L L. Flow field mapping of carbon dioxide nozzle expansion into vacuum[R]. 1985.
[34]. George J, Boyd I. Simulation of nozzle plume flows using a combined CFD-DSMC approach[C]//33rd Thermophysics Conference. 1999: 3454.
[35]. Long W, Wei Y, Xu K. Nonequilibrium flow simulations using unified gas-kinetic wave-particle method[J]. AIAA Journal, 2024, 62(4): 1411-1433.
[36]. Du X, Shi Y, Yang Q, et al. Numerical simulation of spectral radiation for hypersonic vehicles[J]. Aerospace, 2024, 11(10): 802.
[37]. Babou Y, Rivière P, Perrin M Y, et al. High-temperature and nonequilibrium partition function and thermodynamic data of diatomic molecules[J]. International Journal of Thermophysics, 2009, 30(2): 416-438.
[38]. Gamache R R, Vispoel B, Rey M, et al. Total internal partition sums for the HITRAN2020 database[J]. Journal of Quantitative Spectroscopy and Radiative Transfer, 2021, 271: 107713.
[39]. Dubuet U, Pannier E, Laux C O. Uncertainties in multi-temperature nonequilibrium partition functions and

application to CO2[J]. Journal of Quantitative Spectroscopy and Radiative Transfer, 2022, 290: 108314.

[40]. Laux C O. Radiation and non-equilibrium collisional-radiative models[C] // Physico-Chemical Modeling of High Enthalpy and Plasma Flows. Von Karman Institute Lecture Series 2002-07. Rhode-Saint-Genèse: von Karman Institute, 2002.

[41]. Ludwig C B, Malkmus W, Reardon J E, et al. Handbook of infrared radiation from combustion gases[R]. 1973.